CHEMISTRY OF MATERIALS

pubs.acs.org/cm

Article

Epitaxial Monolayers of the Magnetic 2D Semiconductor $FeBr_2$ Grown on Au(111)

Sebastien E. Hadjadj,[⧖] Carmen González-Orellana,[⧖] James Lawrence, Djuro Bikaljević, Marina Peña-Díaz, Pierluigi Gargiani, Lucia Aballe, Jan Naumann, Miguel Ángel Niño, Michael Foerster, Sandra Ruiz-Gómez, Sangeeta Thakur, Ivar Kumberg, James M. Taylor, Jack Hayes, Jorge Torres, Chen Luo, Florin Radu, Dimas G. de Oteyza, Wolfgang Kuch, José Ignacio Pascual, Celia Rogero, and Maxim Ilyn*

Cite This: *Chem. Mater.* 2023, 35, 9847−9856

Read Online

ACCESS | Metrics & More | Article Recommendations | Supporting Information

ABSTRACT: Magnetic two-dimensional (2D) semiconductors have attracted a lot of attention because modern preparation techniques are capable of providing single-crystal films of these materials with precise control of thickness down to the single-layer limit. It opens up a way to study a rich variety of electronic and magnetic phenomena with promising routes toward potential applications. We have investigated the initial stages of epitaxial growth of the magnetic van der Waals semiconductor $FeBr_2$ on a single-crystal Au(111) substrate by means of low-temperature scanning tunneling microscopy (STM), low-energy electron diffraction (LEED), X-ray photoemission spectroscopy (XPS), low-energy electron emission microscopy (LEEM), and X-ray photoemission electron microscopy (XPEEM). Magnetic properties of the one- and two-layer thick films were measured via X-ray absorption spectroscopy (XAS) and X-ray magnetic circular dichroism (XMCD). Our findings show a striking difference in the magnetic behavior of the single layer of $FeBr_2$ and its bulk counterpart, which can be attributed to the modifications in the crystal structure due to the interaction with the substrate.

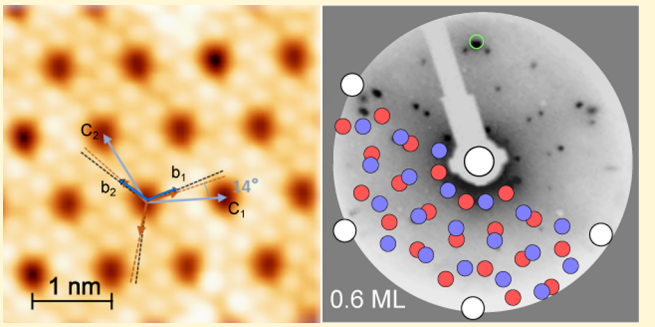

INTRODUCTION

Integration of two-dimensional (2D) materials in technologically relevant applications requires atomic-scale control of the growth of single-crystalline, monolayer-thick films. Meanwhile, many semiconducting 2D materials like graphene, h-BN, or MoS_2 are routinely grown on the wafer scale,[1] but the preparation of magnetic 2D materials is still limited in most cases to micromechanical exfoliation.[2−10] Prominent exceptions of this trend are magnetic transition-metal tri- and dihalides, for which single-layer growth was demonstrated recently via molecular beam epitaxy.[11,12] In contrast to well-studied trihalides, particularly CrI_3 and $CrBr_3$,[2,13−15] experimental investigation of the 2D dihalides is less advanced, although their bulk magnetic properties were thoroughly studied.[16]

Bulk $FeBr_2$ is a layered crystal that consists of covalently bonded layers stacked via van der Waals (vdW) interactions in the CdI_2-type structure ($P3m1$ space group). The layers consist of triangular lattices of cations in edge-sharing octahedral coordination 1T (or D_{3d})- MX_2 structures, forming one transition-metal layer sandwiched between two halide layers.[16,17] The lateral lattice constant was found to be 3.776 Å.[18,19] Indirect Fe−Fe exchange interaction gives rise to a collinear intralayer ferromagnetic order below T_N = 14.2 K with out-of-plane (OOP) anisotropy, while the interlayer exchange is antiferromagnetic. Application of an external magnetic field of 3.15 T triggers a metamagnetic phase transition.[16,20] The six 3d electrons of the Fe^{2+} ions are distributed between two groups of orbitals, t_{2g} (d_{xy}, d_{xz}, and d_{yz}) and e_g ($d_{x^2-y^2}$ and d_{z^2}), giving rise to a magnetic moment of 4.4 ± 0.7 μ_B/Fe atom,[21] which exceeds the value of 4.0 μ_B/Fe atom predicted by Hund's rule.[22,23] Various attempts of density functional theory (DFT) calculations yield comparable values of the magnetic moments and provide useful insights into the details of the band structure.[24−26]

In this work, we use sublimation of the stoichiometric powder to grow epitaxial films of the magnetic semiconductor

Received: April 25, 2023
Revised: November 8, 2023
Accepted: November 9, 2023
Published: November 27, 2023

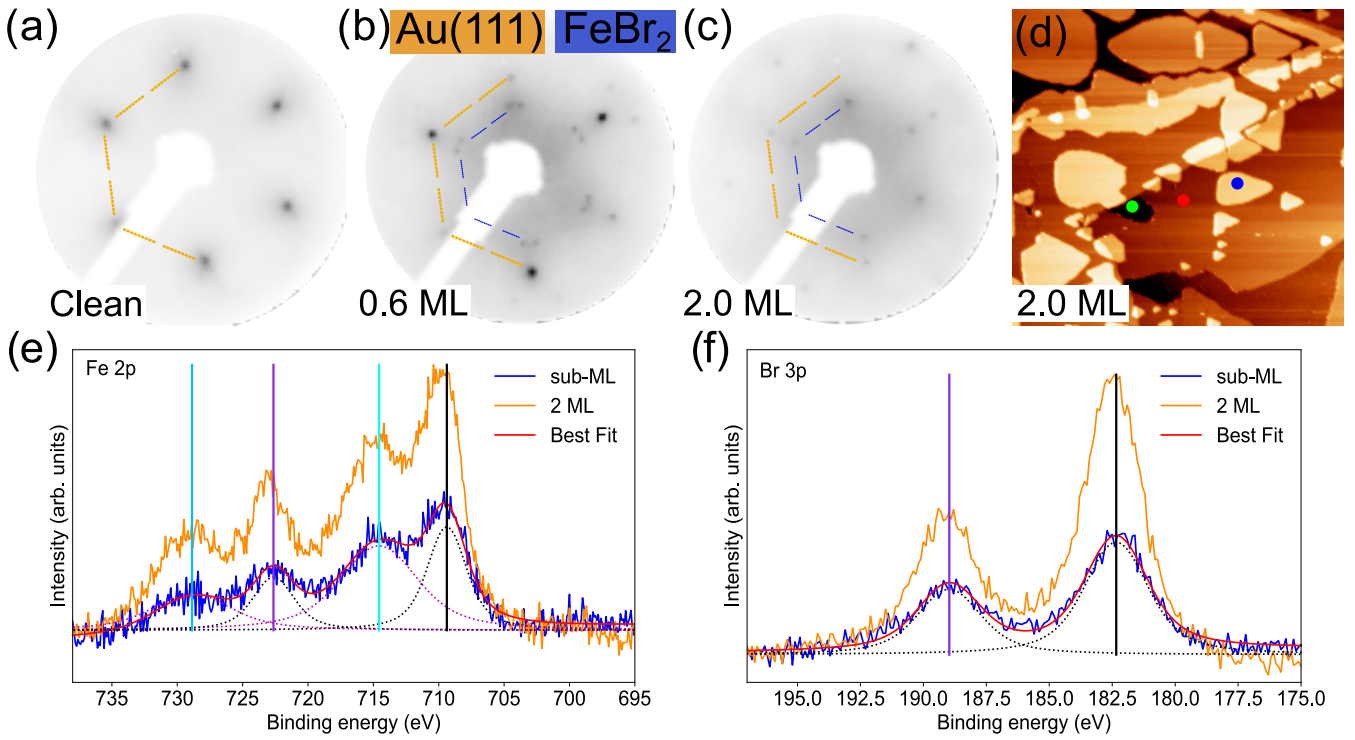

Figure 1. (a–c) LEED images at 137 eV of (a) clean Au(111), (b) submonolayer (0.6 ML) and (c) bilayer (2 ML) of $FeBr_2$ on Au(111). The orange half hexagon is used to designate the pattern of Au(111), and the blue half hexagon marks the pattern of $FeBr_2$. (d) Zoomed-in part of the STM image (Figure S5) of 2.0 ML $FeBr_2$/Au(111), (T = 77 K, U_{Bias} = 1 V and I_{TC} = 0.02 × 10^{-9} A) measured at the BOREAS beamline. The image size is 129.9 × 129.9 nm^2. In one of the terraces, we appended green, red, and blue spots to indicate the levels corresponding to the first, second, and third ML of $FeBr_2$, respectively. (e, f) XPS spectra of 0.6 and 2 ML of $FeBr_2$/Au(111) showing the Fe 2p and Br 3p core levels.

$FeBr_2$, which belongs to the family of transition-metal dihalides (TMDHs)[16] on the single-crystal Au(111). Feasibility of growth of TMDH films via chemical vapor deposition (CVD) has been demonstrated recently.[27] In contrast to CVD, molecular beam epitaxy (MBE) does not require heating of the substrate above room temperature, which makes it compatible with resist-based nanofabrication and opens up a way to the integration of TMDH thin films in the scalable manufacturing processes. We focus our investigation on the properties of the one- and two-slab-thick films employing spectroscopic and microscopic characterization, including synchrotron-based techniques. In particular, we demonstrate the modification of the magnetic properties of the stoichiometric $FeBr_2$ due to a reconstruction in the first slab.

EXPERIMENTS AND METHODS

$FeBr_2$ layers with variable thicknesses, ranging from submonolayer (sub-ML) to more than one monolayer, were grown on Au(111) using $FeBr_2$ powder from Sigma-Aldrich with a purity of 98% and a Knudsen cell evaporator. The sublimation temperature for $FeBr_2$ was around 400 °C in ultrahigh vacuum (UHV) (with an evaporation pressure of 10^{-8} to 10^{-9} mbar). The substrate was kept at room temperature during sublimation. A quartz microbalance was used to measure the nominal amount of the deposited material; meanwhile, the calibration of the absolute thickness was done via cross-correlation of scanning tunneling microscopy (STM) images with low-energy electron diffraction (LEED) data. This calibration was translated to the integral of the nonpolarized soft X-ray absorption at the Fe $L_{3,2}$ edges for comparison to samples prepared in different synchrotron radiation sources. The thickness calibration procedure is shown in the Supporting Information in Figure S2. The Au(111) substrate was cleaned by standard Ar^+ sputtering and annealing cycles. Low-temperature STM (LT-STM) experiments were performed at 4.3 K (for a sub-ML sample) and at 77 K for the thicker samples at Centro de Física de Materiales and the BOREAS beamline, respectively.

X-ray photoelectron spectroscopy (XPS) measurements were carried out with a Phoibos 100 photoelectron spectrometer, using a nonmonochromatic Al–K_α X-ray source. The analyzer energy resolution is 0.1 eV. UHV was preserved during all of the sample transfers (base pressure during the experiment was 10^{-10} mbar).

X-ray magnetic circular dichroism (XMCD) measurements were performed at both the VEKMAG station (dipole-beamline) of BESSY II in Berlin[28] and the BOREAS beamline (undulator-beamline) at ALBA Synchrotron Light Facility.[29] The measurements at VEKMAG were performed by keeping the beam polarization constant and changing the field. At BOREAS, we kept the field constant and changed the polarization. Absorption spectra at the Fe $L_{3,2}$-edges were acquired at normal incidence (NI/0°, out of plane) and grazing incidence (GI/70°, in plane), applying a variable magnetic field up to ±6 T. The temperature during the measurements at the VEKMAG beamline was set to 10 K, which is around 12.6 K and at BOREAS, it was 2 ± 0.5 K. One 0.6 ML sample of $FeBr_2$ was brought by a Ferrovac suitcase to the BOREAS beamline to cross-correlate the coverage of the samples measured in the home laboratory and in the synchrotron beamlines. A control sample with similar coverage was grown in situ and characterized at the BOREAS beamline. XAS/XMCD measurements did not show substantial differences between the samples.

The LEED images were acquired to observe the growth and thickness-dependent changes in the structure. Imaging at the mesoscopic scale was done by low-energy electron microscopy (LEEM) and X-ray photoemission electron microscopy (XPEEM) at the CIRCE beamline (ALBA Synchrotron Light Facility).[30]

RESULTS AND DISCUSSION

Epitaxial Growth of $FeBr_2$. The initial stage of growth of $FeBr_2$ films on single-crystal Au(111) was studied by means of

https://doi.org/10.1021/acs.chemmater.3c00978
Chem. Mater. 2023, 35, 9847–9856

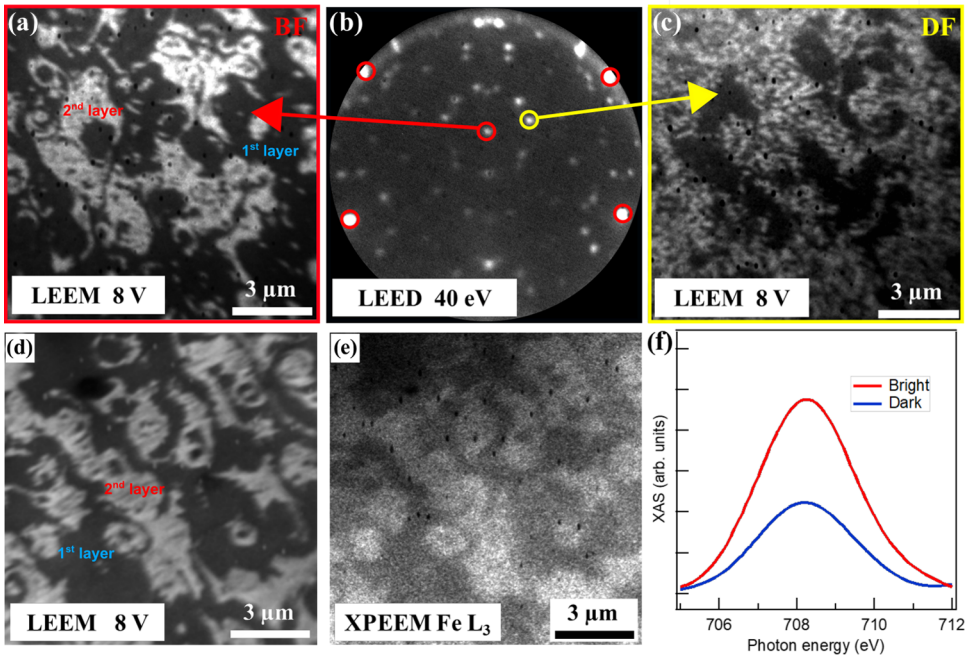

Figure 2. LEEM and XPEEM images of 1.5 ML of $FeBr_2$ on Au(111) at room temperature. (a) Bright-field (BF) LEEM image. (b) μ-LEED pattern at 40 eV; red circles indicate the Au(111) LEED pattern, and the yellow circle marks the spot, belonging to the $FeBr_2$ superstructure that was used for the dark-field (DF) image. The μ-LEED pattern is distorted since the experiment was performed with the microscope working at 10 kV, energy for which the lenses were not completely aligned in the diffraction mode, in order to avoid sparks during imaging. The Au(111) pattern was used as a guide to the eye to correct the distortions. (c) DF-LEEM image taken at the same area as the BF image in panel (a). (d) Bright-field LEEM image in a different area of the sample. (e) XPEEM image at the Fe L_3-edge in the same area as panel (d). (f) Averaged intensities of the bright and dark areas of the XPEEM image, (e), as a function of the X-ray photon energy. The XAS spectra are obtained by averaging the intensity of a certain area across the stack of photon energy dependent images.

surface-sensitive electron diffraction and scanning tunneling microscopy. LEED patterns measured at 137 eV demonstrate a variation of the crystal structure of $FeBr_2$ with an increasing number of deposited layers (Figure 1(a–c)). The hexagonal pattern characteristic of the clean Au(111) surface becomes attenuated, and a new hexagonal pattern with a smaller period and the same orientation appears when 0.6 ML of $FeBr_2$ is grown. An additional complex pattern of multiple dots surrounding the first-order spots of Au(111) is indicative of a surface reconstruction process that is depicted in the atomically resolved STM image (Figure 3). In the LEED pattern acquired for the 2 ML sample, the Au(111) signal is barely visible and the reconstruction-related superstructure is strongly attenuated. At this coverage, the hexagonal pattern of the ordered $FeBr_2$ becomes a dominant motif, also seen as second-order diffraction spots. This behavior is characteristic of epitaxial, close to layer-by-layer growth of the overlayers on single-crystal substrates. The large-scale STM image shown in Figure 1(d) (see also Figure S5) demonstrates that the islands of $FeBr_2$ have triangular shapes and well-defined common directions of the symmetry axes. It corroborates well with the ordered epitaxial growth inferred from the LEED diffraction patterns. One can distinguish large areas of the same thickness and limited amount of exposed atomic planes that discard a three-dimensional (3D) growth mode. However, in the sample with a nominal amount of 2.0 ML, there is nucleation of islands of the third layer and, at the same time, some voids exposing the first layer, which leads to the conclusion that the growth does not proceed in a perfect layer-by-layer mode. Figure 1(d) also shows islands of $FeBr_2$ that grow over the atomic step of the substrate. This behavior was reported earlier for a number of different 2D materials.[31−34]

The chemical composition of the films was probed by using XPS measurements. Survey spectra (not shown) show no traces of oxygen or other contamination. The Fe 2p and Br 3p spectra acquired for the 0.6 ML and 2.0 ML samples as well as the calculated best-fitting curves are represented in Figure 1(e,f). For the data evaluation, a Shirley background was subtracted and the peaks were fitted with a combination of Voigt functions (Python lmfit routine[35]). The shape of the Fe 2p spectra closely resembles the spectrum of Fe^{2+} reported for thin insulating films of FeO[36,37] and $FeCl_2$.[38] In total, four Voigt profiles were needed to fit these spectra: two for the main Fe^{2+} peaks and two for the satellite peaks. The main peaks of the Fe 2p core level are located at a binding energy of 709.4 eV for Fe $2p_{3/2}$ and 722.6 eV for Fe $2p_{1/2}$ with a spin−orbit (SO) splitting of ∼13 eV, in close accordance with the data reported in the literature.[36] The satellites are associated with the final-state effect and are related to the multiplet structure of the 2p transition-metal core level.[39] The Br 3p doublet is similar to the spectrum reported for Br^{1-} in KBr, and the position of the peaks falls in the same range of energies.[40] For further information about the fitting parameters, see Table S1. Both Fe 2p and Br 3p spectra have the same shape for the 0.6 ML and 2.0 ML samples. In contrast to the situation observed for $NiBr_2$, XPS spectra of the first layer of $FeBr_2$ have no additional components that could be interpreted as its partial decomposition.[12] Fitting of the Fe 2p spectra for both samples yielded the same parameters (fwhm and center position). Variation of the fwhm for the Br 3p peaks (see Table S1) can be attributed to the different environment of the

https://doi.org/10.1021/acs.chemmater.3c00978
Chem. Mater. 2023, 35, 9847−9856

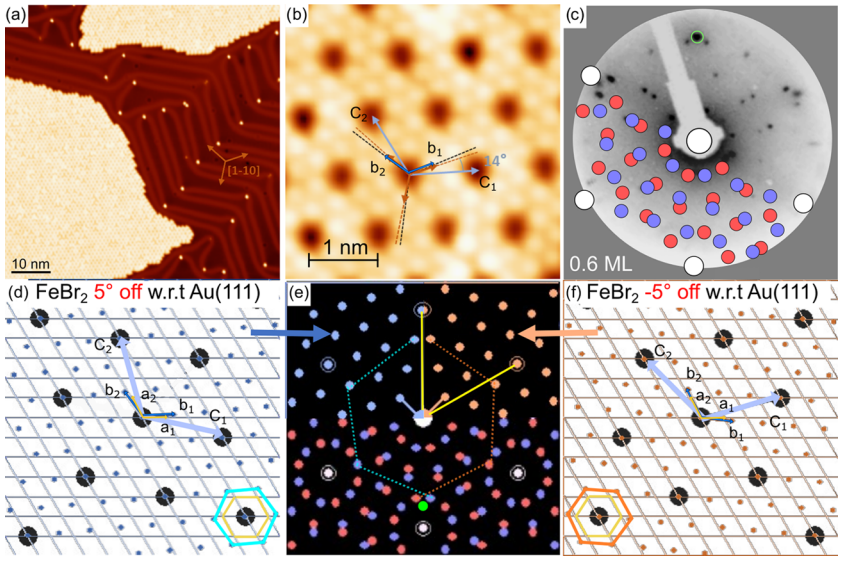

Figure 3. (a, b) STM images of 0.6 ML of $FeBr_2$ at 4.3 K, measured at (a) U_{Bias}= 1 V and I_{TC}= 0.1 nA and (b) U_{Bias} = 1 mV and I_{TC}= 1 nA. Brown arrows indicate the close-packed Au[1 $\bar{1}$0] and equivalent directions. The superstructure unit cell (light-blue arrows) and the hexagonal Br lattice unit cell (black lines) are rotated with respect to the substrate high-symmetry directions. (c) LEED pattern of a 0.6 ML sample measured at 43 eV, partially overlaid with the simulated pattern. The blue and red spheres represent the two rotational domains of the superstructure. The green circle marks one of the spots belonging to the second-layer $FeBr_2$ hexagonal pattern. (d) Relative orientation of Au(111) and rotated Br atomic nets. The lines represent at each crossing point the position of a Au atom, the blue dots represent the Br atoms, and the dark discs mark the coincidence points (a, b, and C are used to designate the respective unit-cell vectors). (e) Simulation of the LEED pattern of Au(111) and of the two symmetric domains of the superstructure. Yellow lines point to the Au(111) pattern, while the dashed lines show the patterns of $FeBr_2$ for both domains. Their relative orientation represents the configurations illustrated by two hexagons in the bottom-right and bottom-left corners of panels (d, f). The green dot shows the position of a spot belonging to the hexagonal pattern of the second layer of $FeBr_2$. (f) is the same as in (d) but the Br grid is rotated in the opposite direction.

bottom Br layer interfaced with the Au(111) surface and higher Br layers.[31] The peak ratio between the main and the satellite peaks as well as the calculated ratio for Br and Fe remains constant for both samples, supporting the presence of one single stoichiometric phase of $FeBr_2$ in the ordered layers epitaxially grown on Au(111).

The uniform epitaxial growth was also verified on the mesoscopic scale via LEEM and XPEEM measurements performed at room temperature. We use the capability of LEEM microscopy and XPEEM to provide information on images with structural and chemical contrast[41] to study the 1.5 ML sample that was grown in situ in the preparation chamber of the microscope. The bright-field LEEM image (the image obtained with a specular-00 spot) is shown in Figure 2(a). The contrast arises from the difference in the local reflectivity of the film with variable thickness.[41] The image represents one complete layer and large, μm-scale islands of the second layer in close accordance with the results of the STM measurements (Figures 1(d) and S5). For identification of the layers, we make use of the reconstruction, characteristic of the first layer of $FeBr_2$/Au(111). The pattern acquired for the 1.5 ML sample with 40 eV energy of electrons (Figure 2(b)) is a superposition of the complex LEED pattern shown in Figure 1(b) and the hexagonal pattern in Figure 1(c), originating from the second layer of $FeBr_2$. The presence of the first-order Au(111) spots shows that the first layer of $FeBr_2$ is not perfectly continuous. Selecting a diffracted beam from the $FeBr_2$ superstructure, i.e., centering the illumination deflectors at that LEED spot, a dark-field image in real space was formed (Figure 2(c)). It has an inverted contrast with respect to the BF image in Figure 2(a). The areas with a higher intensity are those that feature the reconstruction LEED pattern (the first layer of $FeBr_2$). Variation of contrast within the bright zones occurs because of the presence of two rotational domains inside of the first layer of $FeBr_2$ (see the discussion related to Figure 3). The large dark areas display no reconstruction. To prove that these are indeed the areas occupied by 2 ML of $FeBr_2$ but not the pure Au(111), BF LEEM (Figure 2(d)) and XPEEM (Figure 2(e)) images were acquired at the same position.

Again, the specular (00)-spot of the LEED pattern was used for the LEEM measurements; therefore, the contrast in Figure 2(a),(d) is the same. The XPEEM image shows the local difference in X-ray absorption at the Fe L_3-edge. The average intensities of the bright and dark zones were calculated and are represented in Figure 2(f) as a function of the X-ray photon energy. A larger absorption peak characteristic of the bright zones in the XPEEM image proves a higher thickness of the $FeBr_2$ in these areas and consequently in the bright areas of the BF LEEM images (Figure 2(a),(d)). Combining these results with our previous observations, we can conclude that the results of the LEEM/XPEEM characterization corroborate the fact that the growth of $FeBr_2$ on Au(111) is close to the layer-by-layer mode.

Investigation of the atomic arrangement that gives rise to the reconstruction of the first layer of $FeBr_2$/Au(111) was performed using LT-STM and LEED. The STM image displayed in Figure 3(a) shows two islands of $FeBr_2$ separated by the bare Au(111) surface with the characteristic $22 \times \sqrt{3}$ herringbone reconstruction.[42,43] Apart from bright dots at the elbows of the herringbone probably associated with the initial nucleation of $FeBr_2$, the Au(111) remains clean and the $FeBr_2$ grows as compact ordered islands. A zoomed-in image in Figure 3(b) reveals details of a superstructure in the first layer

https://doi.org/10.1021/acs.chemmater.3c00978
Chem. Mater. 2023, 35, 9847−9856

of $FeBr_2$/Au(111) with atomic resolution. It consists of a triangular net of dark spots with a periodicity of 9.7 ± 0.72 Å that obscures single Br atoms in an otherwise flat layer.

Interatomic distances in the topmost Br layer were found to be of 3.66 ± 0.3 Å, in reasonable agreement with the expected monolayer lattice constant calculated by DFT[25] and the bulk value of 3.78 Å for $FeBr_2$[18] (see also Figure S4). The angle between the closed-packed directions of Au(111) and of the topmost Br plane is ∼5°, while the angle between the high-symmetry directions of the Au(111) and the lattice vectors of the superstructure is ∼14°. Figure 3(b) shows that the unit vectors c_1 and c_2 of the reconstruction can be represented in terms of the unit vectors b_1 and b_2 of the Br plane as

$$\begin{pmatrix} c_1 \\ c_2 \end{pmatrix} = \begin{pmatrix} 2 & -1 \\ 1 & 3 \end{pmatrix} \cdot \begin{pmatrix} b_1 \\ b_2 \end{pmatrix} \quad (1)$$

where we drop the vector sign. Although the top and bottom Br planes in the 1T structure of a single $FeBr_2$ slab are not equivalent, they have the same orientation of the high-symmetry directions and their lateral positions can be obtained by a rigid shift along the b_1-b_2 direction. For the sake of clarity, we do not distinguish the top from the bottom Br planes considering the relative orientation of the Br and Au(111) layers, keeping in mind this relative shift.

In Figure 3(d), the Au(111) plane is represented by two series of equally spaced parallel lines, crossed at 120°, and the Br plane is displayed as the set of ordered dots with a 6-fold symmetry. The angle between the close-packed directions of these layers is set to 5°. It is clearly seen that vectors c_1 and c_2 constructed in accordance with eq 1 point to the places of coincidence between the Au(111) and Br layers. Using the unit vectors a_1 and a_2 of the Au(111) plane, they can be represented in a matrix form as

$$\begin{pmatrix} c_1 \\ c_2 \end{pmatrix} = \begin{pmatrix} 3 & -1 \\ 1 & 4 \end{pmatrix} \cdot \begin{pmatrix} a_1 \\ a_2 \end{pmatrix} \quad (2)$$

These points and the equivalent ones are marked with large dark discs in Figure 3(d). Calculations presented in the Supporting Information show that exact coincidence requires rotation of the Br layer by 5.21° and lateral expansion of $FeBr_2$ by ∼3% with respect to the bulk value.

The symmetry of the system requires the existence of $FeBr_2$ islands rotated by the same angle with respect to Au(111) but in the opposite direction. This situation is shown in Figure 3(f). Representation of the unit vectors $\tilde{c}_1$ and $\tilde{c}_2$ of the coincidence points in terms of the unit vectors of the Br plane $\tilde{b}_1$ and $\tilde{b}_2$ as well as the unit vectors of the Au(111) a_1 and a_2 looks like

$$\begin{pmatrix} \tilde{c}_1 \\ \tilde{c}_2 \end{pmatrix} = \begin{pmatrix} 3 & 1 \\ -1 & 2 \end{pmatrix} \cdot \begin{pmatrix} \tilde{b}_1 \\ \tilde{b}_2 \end{pmatrix} = \begin{pmatrix} 4 & 1 \\ -1 & 3 \end{pmatrix} \cdot \begin{pmatrix} a_1 \\ a_2 \end{pmatrix} \quad (3)$$

Figure 3(e) shows a simulation of the LEED pattern by means of the LEEDpat software.[44] We used Au(111) as a substrate, and the superstructure visible in the STM image (Figure 3(b)) as the dark dots was represented by an artificial overlayer. The Au(111) unit-cell size was taken to be 2.86 Å. The overlayers were defined using matrix relations eqs 2 and 3, respectively. Results of the simulation for each domain are shown in the top-left and top-right quarters of Figure 3(e), while the bottom half of the figure shows a superposition of both patterns. We can clearly see the characteristic 12-point circles around the central and the first-order Au(111) spots observed in Figures 1(b) and 2(b). A 43 eV LEED pattern taken for the 0.6 ML $FeBr_2$/Au(111) sample is shown in Figure 3(c). This is the same sample that was used to obtain the LEED data in Figure 1(b), but the superstructure pattern is much more pronounced here because of the lower energy of electrons. Half of the image is overlaid by the simulated pattern of the superstructure. An additional point highlighted with a light-green circle belongs to the hexagonal pattern of the second layer of $FeBr_2$ (corresponding patterns in Figure 1(b), (c) are marked with a blue hexagon). Since the domains of the reconstructed first layer of $FeBr_2$ are rotated by ±5° with respect to the gold lattice, but the second layer grows aligned with the substrate, and since atomically resolved STM images of the second and third layers of $FeBr_2$ shown in Figure S8 display no signs of the reconstruction of the underlying layer, we conclude that the superstructure disappears upon the growth of the higher layers.

The dark spots observed in the STM image (Figure 3(b)) either represent some sort of defects that follow the period of the coincidence points between the Au(111) lattice and the Br lattice of the first $FeBr_2$ layer or can be a pure electronic effect arising due to the interaction between the Br and Au atoms at the interface. Defects in the isostructural compound $FeCl_2$, which were simulated[45] and studied experimentally,[38] have a different appearance. We observed similar objects as in ref 38 randomly distributed within the first layer of $FeBr_2$/Au(111) (see Figures S4 and S6(b)). Although we were unable to measure the band gap, our STS data (Figure S6(a)) show a bump situated at 0.4 eV with respect to the Fermi level that we interpret as the onset of the conduction band (CB); meanwhile, the valence band is below the range of our measurements (−2 eV). Therefore, we suggest that a monolayer of $FeBr_2$/Au(111) is an insulator. In this case, screening of the charge imbalance that would be the consequence of an atomic vacancy would be impeded, and such a defect would affect the electronic state of the surrounding atoms. Indeed, this effect was visualized in the STM image (Figure S6(b)) and the corresponding conductance map, displayed in Figure S6(c). Furthermore, if these spots were defects, we would expect some random imperfections in their ordered structure, unavoidable in any real system, which were never seen in our STM data. On the other hand, STM images of the reconstructed first layer of $FeBr_2$/Au(111) obtained at different values of the bias voltage do not show any change of contrast that we would expect if the dark dots of reconstruction were a purely electronic effect (see Figure S7). Therefore, the mechanism leading to the reconstruction of the first layer of $FeBr_2$/Au(111) is not yet defined and requires further investigation.

Magnetic Properties. Magnetic properties of the in situ-grown single- and double-slab films were measured via XAS/XMCD using circularly polarized synchrotron X-ray radiation. White-line (average of the spectra with left and right polarization) absorption spectra at the Fe L_3 edge aligned to the maximum of the peak and the respective XMCD spectra are shown in Figure 4. The structure of the XAS peak closely resembles the Fe L_3 XAS spectrum measured for $FeCl_2$,[46] which was attributed to the Fe^{2+} oxidation state[47,48] (see also Figure S11). It does not vary either with thickness or with temperature, which confirms the observation from the analysis

https://doi.org/10.1021/acs.chemmater.3c00978
Chem. Mater. 2023, 35, 9847−9856

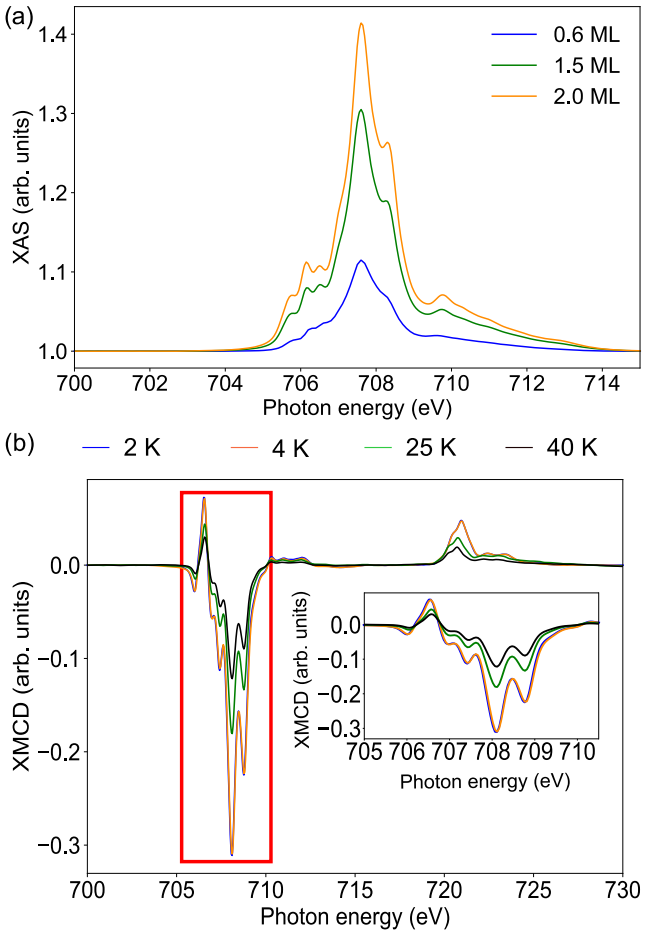

Figure 4. (a) White-line XAS spectra for different thicknesses measured at the Fe L_3-edge, 6 T, 2 K, and NI. The spectra are shifted along the energy axis to align the position of the Fe L_3 peak maxima. Further information about the shift corrections is available in the Supporting Information, Figure S10. The background subtraction was performed by using asymmetrically reweighted penalized least-squares smoothing.[49] (b) XMCD spectra of 2.0 ML of $FeBr_2$ on Au(111) measured at 6 T and NI for different temperatures. The inset image is a zoomed-in version of the L_3 region. All measurements displayed in (a, b) were performed at the BOREAS beamline.

of the XPS data that the films are uniform, single-phase, and contain Fe^{2+} ions in the same coordination.

XMCD magnetization curves measured for different thicknesses at 2 K in two different geometries, normal incidence (NI) and grazing incidence (GI), are shown in Figure 5(a,b). Since they were measured in the total electron yield (TEY) mode, the curves have artifact spikes around 0 T, which were removed. The loops are normalized to the Fe L_3 peak height of the respective white-line (2 K, NI or GI) spectra, and therefore, the intensity values are proportional to the projection of the thermal average of the magnetic moment per Fe atom on the X-ray beam direction at the 6 T field. The corresponding XMCD spectra are displayed as the insets in Figure 5(a,b). The loops do not show any field hysteresis outside the range affected by TEY artifacts, and magnetization vanishes close to zero field, implying that the samples possess no simple collinear ferromagnetic ordering at that temperature.

It was demonstrated in the previous section that the growth of $FeBr_2$ is close to the layer-by-layer mode. Therefore, the 0.6 ML sample comprises mainly one-layer-thick islands, while the 1.5 and 2.0 ML samples consist of the complete first slab and islands of the second and, in minor proportion, of the third slab (see also the STM images of the 1.5 and 2.0 ML samples acquired at the beamline, Figure S5). It is clearly seen from the loops in Figure 5 that the expectation value of the magnetization at 2 K and 6 T along the beam direction is substantially lower in the first layer than that in the thicker films. Different sub-ML samples were grown directly at the beamline and compared to the sample transferred via the suitcase. Therefore, we can exclude that the reduced magnetization is a result of contamination since all samples, also the ones grown directly at the beamline, showed a strongly reduced magnetization. Sum-rule analysis of the spectra yields values of the spin magnetic moment close to 1 μ_B for the 0.6 ML sample and about 2 μ_B for the 1.5 and 2.0 ML samples (see Table 1).

Analysis of a heterogeneous magnetic system is complicated; nevertheless, we can infer some additional information about magnetic ordering in the thin films of $FeBr_2$ from the temperature dependence of their magnetic properties. Figure 5 shows in panels (c) and (d) the expectation value of the spin magnetic moment of the 2.0 ML sample and its inverse as a function of temperature (respective values are listed in Table S4), as obtained by sum-rule analysis of the spectra at 6 T. In the paramagnetic state, $1/m_{total}$ is proportional to the susceptibility measured in the field of 6 T, provided that the temperature is high enough to yield a linear magnetization curve. In Figure S13, we show that for Brillouin functions with $J = 2$ and $T \geq 17$ K, this is approximately the case. Linear fitting of the high-temperature part of this curve yields an extrapolated ordering temperature of ~ -10 K, well below the value of 3.5 K reported for the bulk material.[16] Its negative sign indicates the possibility of antiferromagnetic behavior. Although a nonzero value of the extrapolated ordering temperature cannot serve as an unambiguous proof, it implies that the 2.0 ML sample can be magnetically ordered at 2 K. Panel (a) of Figure S12 shows the same total magnetic moments of the 2.0 ML sample together with curves calculated using the Brillouin function. We observe a slope change of the m_{total} vs T curve at ~7 K, in contrast to the behavior expected from a paramagnetic system with $S = 2$, supporting the presence of magnetic correlations in the 2.0 ML sample.

The magnetic behavior of the single-layer $FeBr_2$ is distinctly different. Low values of the magnetic moments in an external field of 6 T compared to the thicker films (Table 1) and shallow magnetization loops in both NI and GI directions (Figure 5) imply a magnetic order that is neither paramagnetic nor ferromagnetic. Figure S12 demonstrates that fitting of the NI 0.6 ML sample's loop to the Brillouin function does not yield satisfactory results. The paramagnetic curve at 2 K is steeper than that of the experimental loop and has a smaller tangent in the high-field regions. Including out-of-plane anisotropy in the model of the paramagnetic system would make its loop even steeper. Therefore, a mere lack of magnetic order cannot explain the observed magnetic properties of a single layer of $FeBr_2$. STM data show that the 0.6 ML $FeBr_2$/Au(111) sample comprises single-layer islands with a lateral size of ~100 nm (see Figure 3). These islands are large enough to neglect the effect of thermal excitations at 2 K and to discard the superparamagnetic behavior. Although recent neutron diffraction data unveiled some clues of a noncollinear magnetic order in bulk $FeBr_2$,[50,51] neither these nor older works[21] showed antiferromagnetic order within the layers of $FeBr_2$. At

https://doi.org/10.1021/acs.chemmater.3c00978
Chem. Mater. 2023, 35, 9847−9856

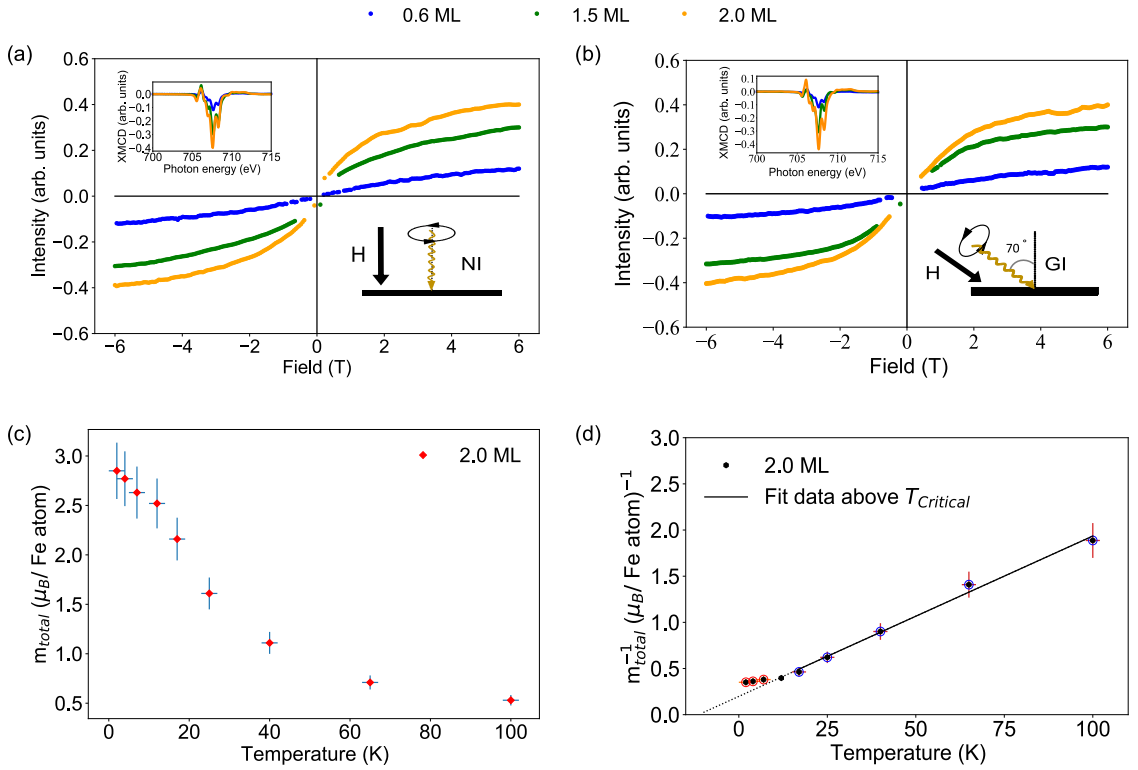

Figure 5. Comparison of the XMCD magnetization loops for 0.6, 1.5, and 2.0 ML $FeBr_2$/Au(111) films measured at 2 K at (a) normal incidence (NI) and (b) grazing incidence (GI) at the Fe L_3-edge, with the field (H) parallel to the beam direction. The magnetization curves are normalized to the respective white-line (averaged $(\sigma^+ + \sigma^-)/2$) XAS peak height. The inset shows the corresponding Fe L_3 XMCD peaks at 6 T and 2 K normalized to the isotropic XAS edge jump for all three samples. The magnetization loops are normalized to the maximum intensity at 6 T and multiplied by the XAS edge-jump height of the L_3-edge. Calculated total moment from the spectra of the 2.0 ML sample at 6 T and NI (c) and its inverse (d) for different temperatures. The hollow blue circles represent the data that were used for the linear fit of the high-temperature regime (17−100 K > $T_{Critical}$). The excluded data points are displayed in red. A slope of 0.017 ± 0.001 (K·μ_B/Fe atom)$^{-1}$ and a linear intercept of −0.198 ± 0.049 (μ_B/Fe atom)$^{-1}$ (χ^2 = 0.01) give the estimation of the paramagnetic Curie temperature of −10 ± 1 K. The chosen temperature range for the performed fit was based on the fact that the lowest used temperature is far away from saturation of a Brillouin function in a J = 2 system. At 17 K, x would be 1.9 (not in saturation; see Figure S13). All measurements displayed in (a, b) were performed at the BOREAS beamline.

Table 1. Magnetic Moments Calculated by Means of the Sum Rules from XMCD Spectra Obtained at T = 2 K and B = 6 T[a]

		μ (μ_B/Fe atom)			
		NI		GI	
ML	T (K)	m_{Seff}	m_l	m_{Seff}	m_l
0.6	2	1.13	0.30	1.05	0.36
1.5	2	1.814	0.60	2.03	0.45
2.0	2	2.15	0.70	1.91	0.47

[a]Magnetic moments (μ) are divided in two sections for NI and GI. The error for each magnetic moment is ±10%. More details about the procedure of sum-rule analysis and the extended version of the data (Table S4) are available in the Supporting Information

the same time, the intralayer exchange coupling to the nearest neighbor J_1 was found to have a different sign with respect to the next-nearest neighbor exchange coupling constant J_2.[50] These competing interactions lead to frustration, which, according to theoretical calculations,[52] can result in complex magnetic textures. The phase diagram presented in ref 52 demonstrates that the magnetic structure varies with the change of the J_1/J_2 ratio or due to modification of the anisotropy. Since the superstructure observed in the first layer of $FeBr_2$/Au(111) causes lateral expansion of the $FeBr_2$ crystal lattice by ∼3% (according to our model) and the super-exchange interaction depends strongly on the angle between the Fe−Br−Fe bonds, variation of the J_1/J_2 ratio can be sufficient to stabilize one of the magnetic textures predicted in ref 52. On the other hand, more complex situations including a spin-glass phase or complex antiferromagnetic ordering cannot be ruled out. Although, among different possible reasons for the distinctive magnetic behavior observed in the single layer of $FeBr_2$, formation of noncollinear magnetic texture due to frustration looks rather probable, further investigations are necessary to unambiguously establish the type of magnetic structure.

SUMMARY

Thin films (sub-ML to 2.0 ML) of $FeBr_2$ were grown epitaxially on a single-crystal Au(111) substrate in UHV via sublimation of the stoichiometric powder compound from a Knudsen cell. Thorough characterization performed by means of XPS and XAS/XMCD spectroscopy as well as via surface-sensitive LEED and LT-STM, LEEM, and XPEEM shows that $FeBr_2$ maintains its stoichiometric chemical composition down to the single-layer limit. The growth of the films is close to the layer-by-layer mode. The first layer of $FeBr_2$/Au(111) demonstrates an atomic reconstruction that is interpreted as the coincidence pattern between the lattice of Br atoms in ±5° rotated domains of ∼3% laterally expanded $FeBr_2$ and the Au(111) surface lattice.

https://doi.org/10.1021/acs.chemmater.3c00978
Chem. Mater. 2023, 35, 9847−9856

XMCD measurements reveal thickness-dependent magnetic properties of $FeBr_2$. While the temperature behavior of the saturation magnetization of the second and higher layers shows some clues of magnetic ordering, magnetic properties of the single layer of $FeBr_2$ were found to be distinctly different. Shallow magnetization loops at 2 K, lack of saturation, and low magnetization in fields up to 6 T leave a possibility for various interpretations starting from magnetic frustration, characteristic of the triangular lattice of the magnetic Fe atoms, to more complex types of magnetic order or spin-glass behavior. These findings open the prospect for further investigation of the monolayers of the 2D magnetic transition-metal dihalides. In contrast to the trihalide family that features the honeycomb arrangement of the magnetic atoms within the 2D layers, triangular nets of magnetic atoms in TMDH are prone to frustration that leads to degeneracy of the magnetic ground state and potentially may result in stronger response toward external stimuli. This quality might result in a rich variety of interesting physical phenomena and opens a way for using 2D magnetic TMDH compounds in applications.

■ ASSOCIATED CONTENT

Supporting Information

The Supporting Information is available free of charge at https://pubs.acs.org/doi/10.1021/acs.chemmater.3c00978.

$FeBr_2$ crystal structure; thickness calibration via XAS measurements; STM pattern angle calculation; lattice constant measurements; STM measurements at the BOREAS beamline; dI/dV spectra for bare Au(111) and $FeBr_2$; bias-dependent STM measurements of the first layer; STM measurements of the second layer of $FeBr_2$; XPS fitting parameters; oxidation state comparison for Fe^{2+}; calculated magnetic moments via sum rules; and Brillouin function fits and XMCD measurements of the Br L_3 edge (PDF)

■ AUTHOR INFORMATION

Corresponding Author

Maxim Ilyn − *Centro de Física de Materiales (CSIC/UPV-EHU), 20018 Donostia-San Sebastián, Spain;* orcid.org/0000-0002-4052-7275; Email: maxim.ilin@ehu.es

Authors

Sebastien E. Hadjadj − *Freie Universität Berlin, Institut für Experimentalphysik, 14195 Berlin, Germany*

Carmen González-Orellana − *Centro de Física de Materiales (CSIC/UPV-EHU), 20018 Donostia-San Sebastián, Spain*

James Lawrence − *Donostia International Physics Center, 20018 Donostia-San Sebastián, Spain;* orcid.org/0000-0001-5503-8661

Djuro Bikaljević − *CIC nanoGUNE-BRTA, 20018 Donostia-San Sebastián, Spain; Institute of Physical Chemistry, University of Innsbruck, A-6020 Innsbruck, Austria;* orcid.org/0000-0003-3409-7042

Marina Peña-Díaz − *Centro de Física de Materiales (CSIC/UPV-EHU), 20018 Donostia-San Sebastián, Spain;* orcid.org/0000-0001-9309-6272

Pierluigi Gargiani − *ALBA Synchrotron Light Source, 08290 Barcelona, Spain;* orcid.org/0000-0002-6649-0538

Lucia Aballe − *ALBA Synchrotron Light Source, 08290 Barcelona, Spain;* orcid.org/0000-0003-1810-8768

Jan Naumann − *Dahlem Center for Complex Quantum Systems, Freie Universität Berlin, 14195 Berlin, Germany;* orcid.org/0000-0003-4513-5139

Miguel Ángel Niño − *ALBA Synchrotron Light Source, 08290 Barcelona, Spain;* orcid.org/0000-0003-3692-147X

Michael Foerster − *ALBA Synchrotron Light Source, 08290 Barcelona, Spain*

Sandra Ruiz-Gómez − *Max Planck Institute for Chemical Physics of Solids, 01180 Dresden, Germany*

Sangeeta Thakur − *Freie Universität Berlin, Institut für Experimentalphysik, 14195 Berlin, Germany*

Ivar Kumberg − *Freie Universität Berlin, Institut für Experimentalphysik, 14195 Berlin, Germany*

James M. Taylor − *Helmholtz-Zentrum Berlin, 12489 Berlin, Germany; Fakultät für Physik, Technische Universität München, 85748 Garching bei München, Germany*

Jack Hayes − *Freie Universität Berlin, Institut für Experimentalphysik, 14195 Berlin, Germany*

Jorge Torres − *Freie Universität Berlin, Institut für Experimentalphysik, 14195 Berlin, Germany*

Chen Luo − *Helmholtz-Zentrum Berlin, 12489 Berlin, Germany; Fakultät für Physik, Technische Universität München, 85748 Garching bei München, Germany;* orcid.org/0000-0001-6476-9116

Florin Radu − *Helmholtz-Zentrum Berlin, 12489 Berlin, Germany*

Dimas G. de Oteyza − *Donostia International Physics Center, 20018 Donostia-San Sebastián, Spain; Nanomaterials and Nanotechnology Research Center (CINN), CSIC-UNIOVI-PA, 33940 Oviedo, Spain;* orcid.org/0000-0001-8060-6819

Wolfgang Kuch − *Freie Universität Berlin, Institut für Experimentalphysik, 14195 Berlin, Germany;* orcid.org/0000-0002-5764-4574

José Ignacio Pascual − *CIC nanoGUNE-BRTA, 20018 Donostia-San Sebastián, Spain; Ikerbasque, Basque Foundation for Science, 48013 Bilbao, Spain*

Celia Rogero − *Centro de Física de Materiales (CSIC/UPV-EHU), 20018 Donostia-San Sebastián, Spain; Donostia International Physics Center, 20018 Donostia-San Sebastián, Spain;* orcid.org/0000-0002-2812-8853

Complete contact information is available at: https://pubs.acs.org/10.1021/acs.chemmater.3c00978

Author Contributions

⧖S.E.H. and C.G.-O. contributed equally to this work.

Notes

The authors declare no competing financial interest.

■ ACKNOWLEDGMENTS

C.G.-O. and M.P.-D. acknowledge funding of the Ph.D. fellowship from the MPC Foundation. S.E.H. thanks the whole AG Kuch and in particular J. Gördes for help during the BESSY measurements and also the local IT/electronics workshop/fine mechanics workshop teams for their continuous support. In particular, he is very thankful for the possibility to perform some last STM measurements at the PEARL beamline at SLS thanks Dr. Matthias Muntwiler. J.N. thanks the Deutsche Forschungsgemeinschaft (DFG, German Research Foundation) for his funding under project 277101999 - CRC 183. S.T. acknowledges financial support by BMBF through project VEKMAG (BMBF 05K19KEA). P.G. acknowledges

funding from PID2020-116181RB-C32 and FlagEraSOgraph-MEM PCI2019-111908-2 (AEI/FEDER). D.G.O. acknowledges funding by the Spanish MCIN/AEI/10.13039/501100011033 and by the European Union "NextGenerationEU"/PRTR (PID2019-107338RB-C63 and TED2021-132388B−C43). C.R., M.I., C.G.-O., and M.P.-D. acknowledge funding by the European Union's Horizon 2020 research and innovation program (grant agreement No 800923), the Spanish MCIN/AEI/10.13039/501100011033 (PID2020-114252GB-I00, PID2019-107338RB-C63, TED2021-130292B−C42), the Basque Goverment IT1591-22, and by the IKUR Strategy under the collaboration agreement between Ikerbasque Foundation and MPC on behalf of the Department of Education of the Basque Government. C.R., M.I., C.G.-O., and S.E.H. are very thankful for the help during the XMCD and STM measurements of Samuel Kerschbaumer, Andrea Aguirre Baños, and Amitayush Jha Thakur.

REFERENCES

(1) Zhang, L.; Dong, J.; Ding, F. Strategies, Status, and Challenges in Wafer Scale Single Crystalline Two-Dimensional Materials Synthesis. *Chem. Rev.* **2021**, *121*, 6321−6372.
(2) Huang, B.; Clark, G.; Navarro-Moratalla, E.; Klein, D. R.; Cheng, R.; Seyler, K. L.; Zhong, D.; Schmidgall, E.; McGuire, M. A.; Cobden, D. H.; Yao, W.; Xiao, D.; Jarillo-Herrero, P.; Xu, X. Layer-dependent ferromagnetism in a van der Waals crystal down to the monolayer limit. *Nature* **2017**, *546*, 270−273.
(3) Sethulakshmi, N.; Mishra, A.; Ajayan, P.; Kawazoe, Y.; Roy, A. K.; Singh, A. K.; Tiwary, C. S. Magnetism in two-dimensional materials beyond graphene. *Mater. Today* **2019**, *27*, 107−122.
(4) Ashton, M.; Gluhovic, D.; Sinnott, S. B.; Guo, J.; Stewart, D. A.; Hennig, R. G. Two-dimensional intrinsic half-metals with large spin gaps. *Nano Lett.* **2017**, *17*, 5251−5257.
(5) Li, H.; Ruan, S.; Zeng, Y. Intrinsic van der Waals magnetic materials from bulk to the 2d limit: New frontiers of spintronics. *Adv. Mater.* **2019**, *31*, No. 1900065.
(6) Gibertini, M.; Koperski, M.; Morpurgo, A. F.; Novoselov, K. S. Magnetic 2d materials and heterostructures. *Nat. Nanotechnol.* **2019**, *14*, 408−419.
(7) Cortie, D. L.; Causer, G. L.; Rule, K. C.; Fritzsche, H.; Kreuzpaintner, W.; Klose, F. Two-dimensional magnets: Forgotten history and recent progress towards spintronic applications. *Adv. Funct. Mater.* **2020**, *30*, No. 1901414.
(8) Li, W.; Zeng, Y.; Zhao, Z.; Zhang, B.; Xu, J.; Huang, X.; Hou, Y. 2d magnetic heterostructures and their interface modulated magnetism. *ACS Appl. Mater. Interfaces* **2021**, *13*, 50591−50601.
(9) Zhao, Z.; Li, W.; Zeng, Y.; Huang, X.; Yun, C.; Zhang, B.; Hou, Y. Structure engineering of 2d materials toward magnetism modulation. *Small Struct.* **2021**, *2*, No. 2100077.
(10) Huang, Y. L.; Chen, W.; Wee, A. T. S. Two−dimensional magnetic transition metal chalcogenides. *SmartMat* **2021**, *2*, 139−153.
(11) Kezilebieke, S.; Huda, M. N.; Vaňo, V.; Aapro, M.; Ganguli, S. C.; Silveira, O. J.; Głodzik, S.; Foster, A. S.; Ojanen, T.; Liljeroth, P. Topological superconductivity in a van der Waals heterostructure. *Nature* **2020**, *588*, 424−428.
(12) Bikaljević, D.; González-Orellana, C.; Pena-Díaz, M.; Steiner, D.; Dreiser, J.; Gargiani, P.; Foerster, M.; Nino, M. A.; Aballe, L.; Ruiz-Gomez, S.; Friedrich, N.; Hieulle, J.; Jingcheng, L.; Ilyn, M.; Rogero, C.; Pascual, J. I. Noncollinear magnetic order in two-dimensional $NiBr_2$ films grown on Au(111). *ACS Nano* **2021**, *15*, 14985−14995.
(13) Chen, W.; Sun, Z.; Wang, Z.; Gu, L.; Xu, X.; Wu, S.; Gao, C. Direct observation of van der waals stacking-dependent interlayer magnetism. *Science* **2019**, *366*, 983−987.
(14) Huang, B.; Clark, G.; Klein, D. R.; MacNeill, D.; Navarro-Moratalla, E.; Seyler, K. L.; Wilson, N.; McGuire, M. A.; Cobden, D. H.; Xiao, D.; Yao, W.; Jarillo-Herrero, P.; Xu, X. Electrical control of 2d magnetism in bilayer CrI_3. *Nat. Nanotechnol.* **2018**, *13*, 544−548.
(15) Bonilla, M.; Kolekar, S.; Ma, Y.; Diaz, H. C.; Kalappattil, V.; Das, R.; Eggers, T.; Gutierrez, H. R.; Phan, M.-H.; Batzill, M. Strong room-temperature ferromagnetism in VSe_2 monolayers on van der Waals substrates. *Nat. Nanotechnol.* **2018**, *13*, 289−293.
(16) McGuire, M. Crystal and magnetic structures in layered, transition metal dihalides and trihalides. *Crystals* **2017**, *7*, No. 121.
(17) Chhowalla, M.; Shin, H. S.; Eda, G.; Li, L.-J.; Loh, K. P.; Zhang, H. The chemistry of two-dimensional layered transition metal dichalcogenide nanosheets. *Nat. Chem.* **2013**, *5*, 263−275.
(18) Haberecht, J.; Borrmann, H.; Kniep, R. Refinement of the crystal structure of iron dibromide, $FeBr_2$. *Z. Kristallogr. - New Cryst. Struct.* **2001**, *216*, No. 510.
(19) Youn, S. J.; Sahu, B. R.; Kim, K. S. Large orbital magnetic moment and Coulomb correlation effects in $FeBr_2$. *Phys. Rev. B* **2002**, *65*, No. 052415.
(20) Yang, S.; Zhang, T.; Jiang, C. van der Waals magnets: Material family, detection and modulation of magnetism, and perspective in spintronics. *Adv. Sci.* **2021**, *8*, No. 2002488.
(21) Wilkinson, M. K.; Cable, J. W.; Wollan, E. O.; Koehler, W. C. Neutron diffraction investigations of the magnetic ordering in $FeBr_2$, $CoBr_2$, $FeCl_2$, and $CoCl_2$. *Phys. Rev.* **1959**, *113*, 497−507.
(22) Ropka, Z.; Michalski, R.; Radwanski, R. J. Electronic and magnetic properties of $FeBr_2$. *Phys. Rev. B* **2001**, *63*, No. 172404.
(23) Pelloth, J.; Brand, R. A.; Takele, S.; Pereira de Azevedo, M. M.; Kleemann, W.; Binek, C.; Kushauer, J.; Bertrand, D. Local magnetic properties of antiferromagnetic $FeBr_2$. *Phys. Rev. B* **1995**, *52*, 15372−15386.
(24) Kulish, V. V.; Huang, W. Single-layer metal halides MX_2 (X = Cl, Br, I): stability and tunable magnetism from first principles and Monte Carlo simulations. *J. Mater. Chem. C* **2017**, *5*, 8734−8741.
(25) Botana, A. S.; Norman, M. R. Electronic structure and magnetism of transition metal dihalides: Bulk to monolayer. *Phys. Rev. Mater.* **2019**, *3*, No. 044001.
(26) Sargolzaei, M.; Rusz, J. Spin and orbital magnetism of $FeBr_2$: a density functional theory study. *J. Phys.: Condens. Matter* **2008**, *20*, No. 025217.
(27) Jiang, S.; Wang, G.; Deng, H.; Liu, K.; Yang, Q.; Zhao, E.; Zhu, L.; Guo, W.; Yang, J.; Zhang, C.; Wang, H.; Zhang, X.; Dai, J.-F.; Luo, G.; Zhao, Y.; Lin, J. General synthesis of 2d magnetic transition metal dihalides via trihalide reduction. *ACS Nano* **2023**, *17*, 363−371.
(28) Noll, T.; Radu, F. In*The Mechanics of the VEKMAG Experiment*, Proceedings of MEDSI2016, 2017.
(29) Barla, A.; Nicolás, J.; Cocco, D.; Valvidares, S. M.; Herrero-Martín, J.; Gargiani, P.; Moldes, J.; Ruget, C.; Pellegrin, E.; Ferrer, S. Design and performance of BOREAS, the beamline for resonant x-ray absorption and scattering experiments at the ALBA synchrotron light source. *J. Synchrotron Radiat.* **2016**, *23*, 1507−1517.
(30) Aballe, L.; Foerster, M.; Pellegrin, E.; Nicolas, J.; Ferrer, S. The ALBA spectroscopic LEEM-PEEM experimental station: layout and performance. *J. Synchrotron Radiat.* **2015**, *22*, 745−752.
(31) Bana, H.; Travaglia, E.; Bignardi, L.; Lacovig, P.; Sanders, C. E.; Dendzik, M.; Michiardi, M.; Bianchi, M.; Lizzit, D.; Presel, F.; Angelis, D. D.; Apostol, N.; Das, P. K.; Fujii, J.; Vobornik, I.; Larciprete, R.; Baraldi, A.; Hofmann, P.; Lizzit, S. Epitaxial growth of single-orientation high-quality MoS_2 monolayers. *2D Mater.* **2018**, *5*, No. 035012.
(32) Bets, K. V.; Gupta, N.; Yakobson, B. I. How the complementarity at vicinal steps enables growth of 2d monocrystals. *Nano Lett.* **2019**, *19* (3), 2027−2031.
(33) Günther, S.; Dänhardt, S.; Wang, B.; Bocquet, M.-L.; Schmitt, S.; Wintterlin, J. Single terrace growth of graphene on a metal surface. *Nano Lett.* **2011**, *11* (5), 1895−1900.
(34) Yang, P.; Zhang, S.; Pan, S.; Tang, B.; Liang, Y.; Zhao, X.; Zhang, Z.; Shi, J.; Huan, Y.; Shi, Y.; Pennycook, S. J.; Ren, Z.; Zhang, G.; Chen, Q.; Zou, X.; Liu, Z.; Zhang, Y. Epitaxial growth of centimeter-scale single-crystal MoS_2 monolayer on Au(111). *ACS Nano* **2020**, *14* (4), 5036−5045.

https://doi.org/10.1021/acs.chemmater.3c00978
Chem. Mater. 2023, 35, 9847−9856

(35) Newville, M.; Stensitzki, T.; Allen, D. B.; Ingargiola, A. *LMFIT: Non-Linear Least-Square Minimization and Curve-Fitting for Python*, 2014.
(36) Martín-García, L.; Bernal-Villamil, I.; Oujja, M.; Carrasco, E.; Gargallo-Caballero, R.; Castillejo, M.; Marco, J. F.; Gallego, S.; de la Figuera, J. Unconventional properties of nanometric FeO(111) films on Ru(0001): stoichiometry and surface structure. *J. Mater. Chem. C* **2016**, *4* (9), 1850−1859.
(37) Yamashita, T.; Hayes, P. Analysis of XPS spectra of Fe^{2+} and Fe^{3+} ions in oxide materials. *Appl. Surf. Sci.* **2008**, *254*, 2441−2449.
(38) Zhou, X.; Brzostowski, B.; Durajski, A.; Liu, M.; Xiang, J.; Jiang, T.; Wang, Z.; Chen, S.; Li, P.; Zhong, Z.; Drzewiński, A.; Jarosik, M.; Szcześniak, R.; Lai, T.; Guo, D.; Zhong, D. Atomically thin 1T-$FeCl_2$ grown by molecular-beam epitaxy. *J. Phys. Chem. C* **2020**, *124* (17), 9416−9423.
(39) Bagus, P. S.; Nelin, C. J.; Brundle, C. R.; Crist, B. V.; Lahiri, N.; Rosso, K. M. Origin of the complex main and satellite features in Fe 2p XPS of Fe_2O_3. *Phys. Chem. Chem. Phys.* **2022**, *24*, 4562−4575.
(40) Moulder, J. F. *Handbook of X-ray Photoelectron Spectroscopy: a Reference Book of Standard Spectra for Identification and Interpretation of XPS Data*; Perkin-Elmer Corporation, 1992.
(41) Flege, J. I.; Krasovskii, E. E. Intensity-voltage low-energy electron microscopy for functional materials characterization. *Phys. Status Solidi RRL* **2014**, *8* (6), 463−477.
(42) Murphy, C. J.; Shi, X.; Jewell, A. D.; McGuire, A. F.; Bellisario, D. O.; Baber, A. E.; Tierney, H. L.; Lewis, E. A.; Sholl, D. S.; Sykes, E. C. H. Impact of branching on the supramolecular assembly of thioethers on Au(111). *J. Chem. Phys.* **2015**, *142*, No. 101915.
(43) Schouteden, K.; Lievens, P.; Van Haesendonck, C. Fourier-transform scanning tunneling microscopy investigation of the energy versus wave vector dispersion of electrons at the Au(111) surface. *Phys. Rev. B* **2009**, *79*, No. 195409.
(44) Hermann, K.; Van Hove, M. A. Leedpat4: LEED pattern analyzer 2022 https://www.fhi.mpg.de/958975/leedpat4. (accessed September 28, 2022).
(45) Ceyhan, E.; Yagmurcukardes, M.; Peeters, F. M.; Sahin, H. Electronic and magnetic properties of single-layer $FeCl_2$ with defects. *Phys. Rev. B* **2021**, *103*, No. 014106.
(46) Everett, J.; Céspedes, E.; Shelford, L. R.; Exley, C.; Collingwood, J. F.; Dobson, J.; van der Laan, G.; Jenkins, C. A.; Arenholz, E.; Telling, N. D. Ferrous iron formation following the co-aggregation of ferric iron and the Alzheimer's disease peptide β-amyloid (1−42). *J. R. Soc., Interface* **2014**, *11*, No. 20140165.
(47) Kowalska, J. K.; Nayyar, B.; Rees, J. A.; Schiewer, C. E.; Lee, S. C.; Kovacs, J. A.; Meyer, F.; Weyhermüller, T.; Otero, E.; DeBeer, S. Iron $L_{2,3}$ -edge x-ray absorption and x-ray magnetic circular dichroism studies of molecular iron complexes with relevance to the FeMoCo and FeVCo active sites of nitrogenase. *Inorg. Chem.* **2017**, *56*, 8147−8158.
(48) Miedema, P. S.; de Groot, F. M. The iron L edges: Fe 2p x-ray absorption and electron energy loss spectroscopy. *J. Electron Spectrosc. Relat. Phenom.* **2013**, *187*, 32−48.
(49) Baek, S.-J.; Park, A.; Ahn, Y.-J.; Choo, J. Baseline correction using asymmetrically reweighted penalized least squares smoothing. *Analyst* **2015**, *140*, 250−257.
(50) Katsumata, K.; Katori, H. A.; Shapiro, S. M.; Shirane, G. Neutron-scattering studies of a phase transition in the metamagnet $FeBr_2$ under external magnetic fields. *Phys. Rev. B* **1997**, *55*, 11466−11470.
(51) Binek, C.; Kato, T.; Kleemann, W.; Petracic, O.; Bertrand, D.; Bourdarot, F.; Burlet, P.; Katori, H. A.; Katsumata, K.; Prokes, K.; Welzel, S. Neutron scattering study of transverse magnetism in the metamagnet $FeBr_2$. *Eur. Phys. J. B* **2000**, *15*, 35−40.
(52) Leonov, A. O.; Mostovoy, M. Multiply periodic states and isolated skyrmions in an anisotropic frustrated magnet. *Nat. Commun.* **2015**, *6*, No. 8275.

https://doi.org/10.1021/acs.chemmater.3c00978
Chem. Mater. 2023, 35, 9847−9856